Adaptive Subsurface Imaging based on Peak Phase-Profile: The Significance in Separation of Scattering Phase from Propagation Phase

Akira Hirose* and Soshi Shimomura*
* The University of Tokyo, Tokyo, Japan
E-mail: ahirose@ee.t.u-tokyo.ac.jp

***Abstract*—This paper discusses the separation of scattering phase and propagation phase in radar systems. Recently we proposed a novel radar imaging scheme using complex-valued self-organizing map (CSOM) to deal with time-domain phase profile of subsurface targets. Most of conventional radar imaging schemes pays limited attention to phase information. However, we consider that the phase values represent scattering mechanisms while the amplitude peaks indicate scatterers' distance. Then the phase profile is widely useful in grouping for target recognition. In this paper, we discuss the importance of the explicit separation of the scattering phase from the propagation phase. We also refer to the correspondence of this idea to the use of phasor-quaternion self-organizing map (PQSOM) in our polarimetric radar system. The separation is essential more and more in advanced polarimetric-interferometric radar imaging systems in the near future.**

I. Introduction

Stepped-frequency continuous-wave (SFCW) scheme is one of the standard observation configurations in ground penetrating radar (GPR) systems [1]–[4]. Obtained frequency-domain scattering profile is Fourier transformed to a time domain data, called A-scan, showing target distance as a pulse response [2], [5]. By repeating this observation along a line on the earth surface, we visualize the subsurface two-dimensionally with one-dimensional space by one-dimensional time or depth. This is the B-scan. We can also sweep the surface two-dimensionally to obtain a three-dimensional under-ground image, namely C-scan. They are widely used in a variety of application fields such as void detection, pipe visualization and ruin survey [6]–[9].

This paper intends to discuss the meaning and significance of the phase information by focusing on the separation of scattering phase and propagation phase. Most of conventional systems ignore the phase characteristics in the time-domain processing. However, the authors consider that the phase information in the time domain is as meaningful as that in the frequency domain. We often utilize phase spectra in target grouping and recognition [10]–[12]. Some researchers discussed this point [13], [14] and proposed the so-called phase retrieval (PR) method.

Previously, the authors proposed an imaging scheme, namely peak phase-profile complex-valued self-organizing map (PP-CSOM) imaging, in which a complex-valued self-organizing map (CSOM) deals with time-domain phase profiles (PP) for target grouping and visualization [15], [16]. In this scheme, we find peaks in a time-domain amplitude profile, then clip and move (shift) a peak to the time origin ($t = 0$) to remove the phase rotation in the propagation, Fourier-transform zero-shifted peak to obtain frequency-domain amplitude and phase profiles, which are fed to a CSOM for grouping, and we finally obtain a visualized target in the actual space domain [17]. The result reflects the scattering mechanisms of targets such as plastic landmines [18].

The above process separates the scattering-mechanism phase from the propagation phase to cast light on the targets, resulting in a successful visualization even in tough tasks rather than ranging. This treatment is similar to the separation of polarization and propagation phase in polarimetric synthetic aperture radar (PolSAR). Polarization is determined by the phase difference and the amplitude ratio of two orthogonal components of the electric fields. For a given polarization of illumination, the target scattering mechanism determines the polarization to be observed [19], [20]. The scattering phase information is observable separately from the propagation phase without any special separation process [21]. n this sense, however, the polarization has a meaning similar to that of the relative phase. The polarization-related phase is a relative phase, i.e., the difference between those of two orthogonal components, while the propagation phase is an absolute phase working to both the components equally [22]. This thought leads to phasor quaternion (PQ) neural networks (PQNN) [23]. The PQSOM GPR system based on this separation clearly presented a better visualization [24], [25].

Though we pick up a SFCW system in this paper, note that the discussion is applicable directly to traditional pulse radar systems. In principle, their processing is identical because the time-domain information of a pulse radar is equivalent to that in a frequency-domain radar convertible by Fourier transform. In physical implementation, however, SFCW is much easier because it is free from high-peak pulses and, consequently, from nonlinear distortion in electronics and difficulty in amplitude and phase control. SFCW has also a higher signal-to-noise ratio (SNR) since it has larger transmission and observation duration than a pulse radars, which are active only in the pulse duration. These points are very influential to the performance in particular when we focus on the peak phase profiles.

This paper reviews the PPSOM method first to check the

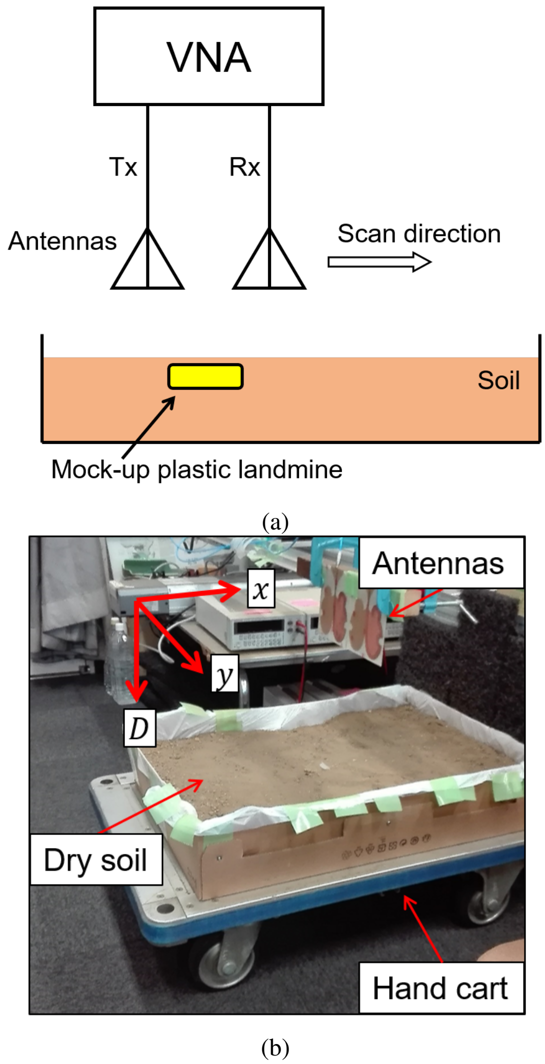

Fig. 1: (a) Conceptual illustration of SFCW GPR measurement setup and (b) a photo of our experiment [15].

features and advantages. Then we discuss its relationship to the PQSOM.

II. Dynamics of Peak Phase-Profile (PP) and CSOM (PP-CSOM) Processing

A. Peak Phase-Profile Extraction

We review the PP-CSOM method. Fig. 1 shows (a) the conceptual illustration of the observation sweeping and (b) the photo of our experiment of the PP-CSOM GPR system. The details are given in Ref. [15], [17]. Fig. 2(a) shows the total signal processing flow while (b) presents the signals at some processing points. The processing is described as follows.

1) Obtain the complex-valued scattering data in the frequency domain $S_{21}(f_n)$ by using a vector network analyzer (VNA).
2) Inversely Fourier transform $S_{21}(f_n)$ to the time-domain complex-valued scattering data. There we can observe a single or multiple peaks (p = 1, 2, ..., p, ... ,P) corresponding to a pulse response, which is shown in Fig. 3 as an A-scan. The time t corresponds to the depth or distance from the transmitting and receiving antennas D.
3) Find major peaks. Clip respective peaks with a window, e.g., Gaussian window.
4) Move a clipped peak to the time origin ($t = 0$) precisely, and apply Fourier transform. The move (shift) removes the propagation phase.
5) Repeat Step 3) and Step 4) for the peaks p, to calculate the scatterers' scattering coefficients $\boldsymbol{k}_p = [\, k_p(f_1)\; k_p(f_2)\; \cdots\; k_p(f_N)\,]^T$ where $[\cdot]^T$ stands for transpose. This profile $\boldsymbol{k}_p$ is the feature vector representing the feature of a voxel.
6) Group the voxels based on their respective feature vectors $\boldsymbol{k}_p$, explained below, by using a CSOM.
7) Designate colors to the voxels in the actual space based on the neuron number (= class number) obtained by the CSOM to visualize targets.

TABLE I: Variables and parameters used in the CSOM processing [15].

$\hat{c}$	winner class
$\boldsymbol{w}_{\hat{c}}(t)$	weight of the winner class neuron $\hat{c}$ (= reference vector)
$\boldsymbol{w}_{\hat{c}\pm 1}(t)$	weight of the neurons next to the winner neuron (= reference vector)
$\boldsymbol{k}$	input feature vector (= frequency profiles of the scattering coefficient)
t	a number of learning of iteration
$\alpha(t)$	self-organizing coefficient of the winner neuron
$\beta(t)$	self-organizing coefficient of the neurons next to the winner neuron ($< \alpha$)

In Step 4), we employ zero-padding in the inverse Fourier transform (IFFT) to increase the window length by ten times to enhance the spatial resolution so high that we can obtain the complex-valued scattering coefficient accurately enough. Step 4) represents the scattering mechanism separately from the propagation characteristics, and we feed this profile to the CSOM as the feature vector.

In contrast, the conventional PR method calculates the average as the feature value calculated as

$$\bar{\theta}_p = \arg\left[\frac{1}{N}\sum_{n=1}^{N} k_p(f_n)\right] = \arg\left[\frac{1}{N}\sum_{n=1}^{N} r_p(f_n)e^{j\theta_p(f_n)}\right] \tag{1}$$

where $r_p(f_n)$ and $\theta(f_n)$ are amplitude and phase at frequency f_n, which construct the feature vector $k(f_n)$ (explained below). There, it was pointed out that the averaging causes the loss of important information, namely the frequency profile, of the scattering coefficient.

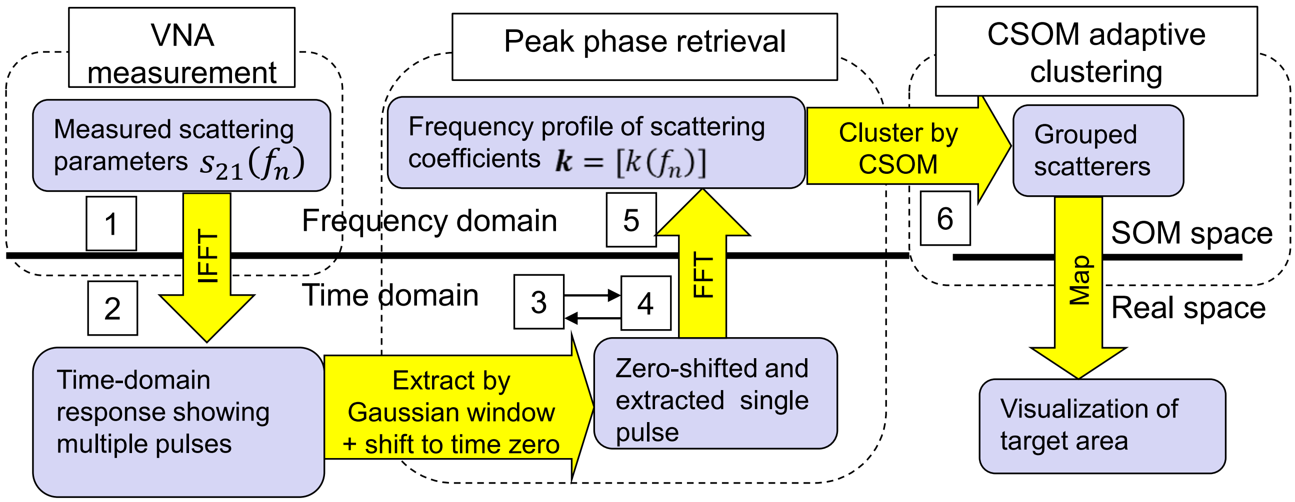

(a)

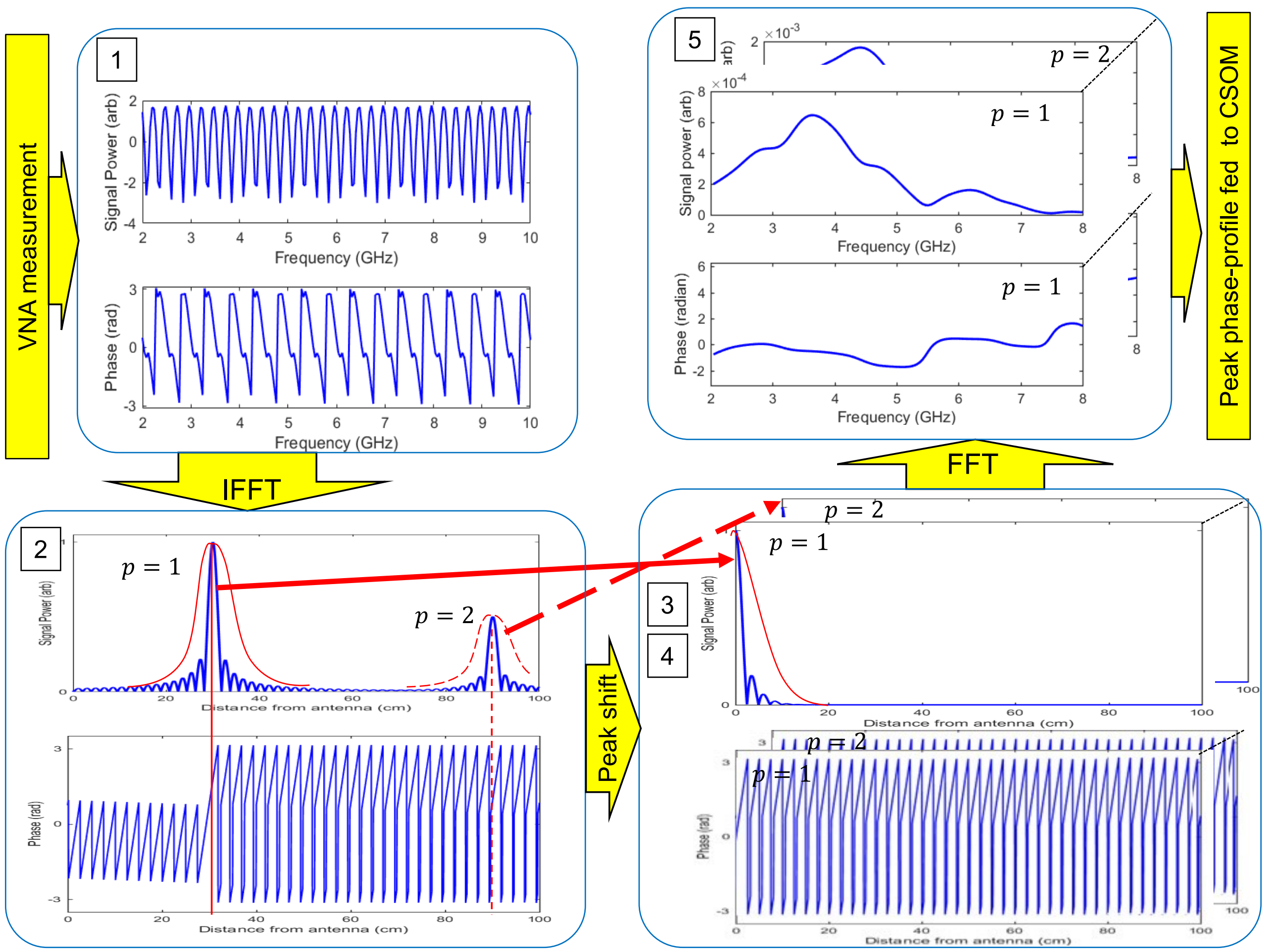

(b)

Fig. 2: (a) Total flow of the signal processing of PP-CSOM and (b) example signals observed at some points.

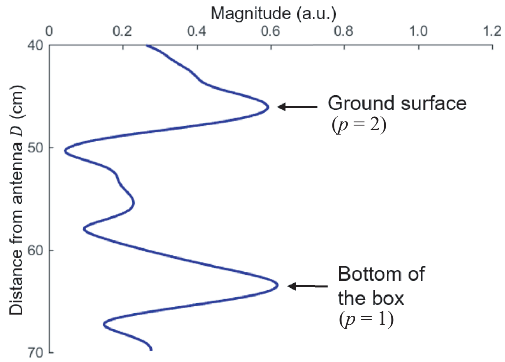

Fig. 3: An A-scan example.

B. Complex-Valued Self-Organizing Map

In our method, we feed the high-dimensional feature vector $\boldsymbol{k}_p(f_n)$, instead of the average, to the CSOM, which performs robust visualization of high-dimensional data. CSOM is a complex-valued framework of self-organizing map (SOM) [26]. The input vector is $\boldsymbol{k}_p$ expressed as

$$\boldsymbol{k}_p = \begin{bmatrix} k_p(f_1) \\ k_p(f_2) \\ \vdots \\ k_p(f_N) \end{bmatrix} = \begin{bmatrix} r_{p\ 1} \exp(j\theta_{p\ 1}) \\ r_{p\ 2} \exp(j\theta_{p\ 2}) \\ \vdots \\ r_{p\ N} \exp(j\theta_{p\ N}) \end{bmatrix} \tag{2}$$

where p is the suffix for peaks. In the proposed system, we use CSOM to obtain a good generalization ability for the complex-valued data constructed by amplitude and phase [27]–[29].

Table I lists the variables and parameters used in the CSOM. To decide the winner, to which an input feature vector $\boldsymbol{k}_p$ is classified, we use complex-valued inner product determined as [30]

$$\left| \boldsymbol{k}_p^H \cdot \frac{\boldsymbol{w_c}}{||\boldsymbol{w_c}||} \right| = \left| \sum_{n=1}^{N} r_{k_n} \exp(j(\theta_{w_{cn}} - \theta_{k_n})) \right| \tag{3}$$

where $(\cdot)^H$ and $||\cdot||$ mean the complex conjugate transpose (Hermitian conjugate) and the norm of a vector. We use a ring-CSOM having one-dimensional topology, which represents the similarity among the frequency profiles in a one-dimensional space without ends. The weight update rule is expressed as [31]

$$\boldsymbol{w}_{\hat{c}}(t+1) = \boldsymbol{w}_{\hat{c}}(t) + \alpha(t)\,(\boldsymbol{k} - \boldsymbol{w}_{\hat{c}}(t)) \tag{4}$$
$$\boldsymbol{w}_{\hat{c}\pm1}(t+1) = \boldsymbol{w}_{\hat{c}\pm1}(t) + \beta(t)\,(\boldsymbol{k} - \boldsymbol{w}_{\hat{c}\pm1}(t)) \tag{5}$$

where $\hat{c}$ and $\hat{c} \pm 1$ denotes the winner and the neighbors.

We have only two neurons (groups) as the neighbors in the ring-CSOM since the number of the total groups here is only 5 to 8. The self-organizing process realizes an adaptive grouping depending on the fed data. At the same time, neighboring two neurons becomes similar in their weights in accordance with the input feature set. The self-organization dynamics is determined by the self-organization parameters α and β. We call this method in total as PP-CSOM (peak phase-profiling and complex-valued self-organizing map).

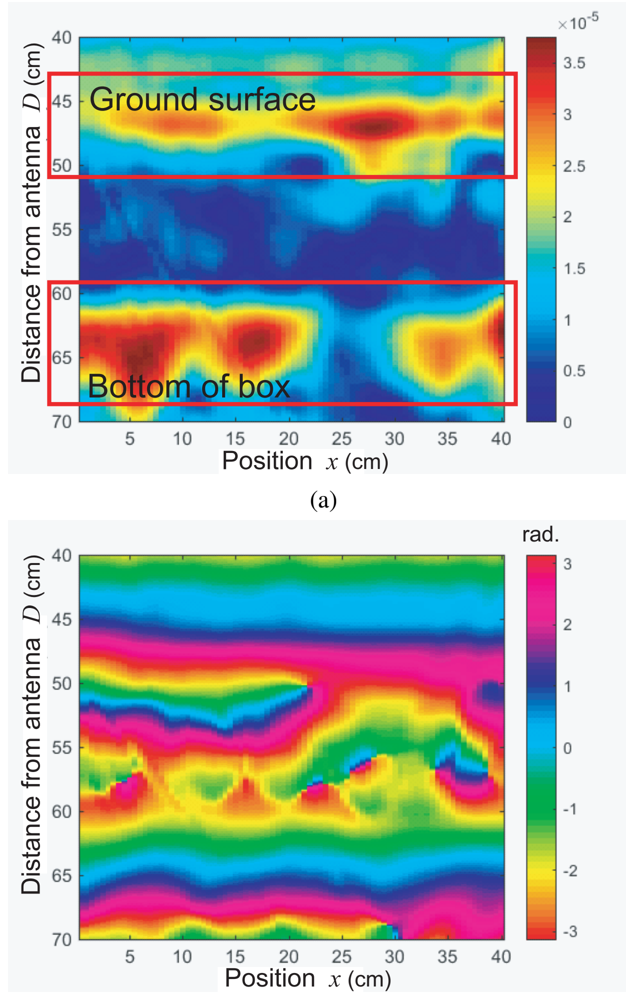

Fig. 4: (a) Amplitude and (b) phase of a B-scan.

III. Result

Fig. 1(b) includes a setup photo. We put mostly dry soil with stones in a big plastic case, and bury a plastic landmine (mock, PMN-2, about 12 cm diameter, 5 cm thickness) at about 1 cm depth. We use taper slot antennas having a wide working frequency range and a high directivity [32]. The number of the frequency points is 101 in 2 to 10 GHz. We move the antennas 30 times in x and y directions, respectively, with 1 cm interval to sweep a 30×30 cm^2 area.

Fig. 3 is an example of A-scan. We find two peaks at D = 47 cm and 64 cm below the antennas. We also obtain a corresponding phase data. Fig. 4 presents the power and phase in a B-scan when we move the antennas in the x direction. Fig. 4(a) shows the amplitude while (b) presents the phase of the equivalent pulse response. In this experiment, there are two

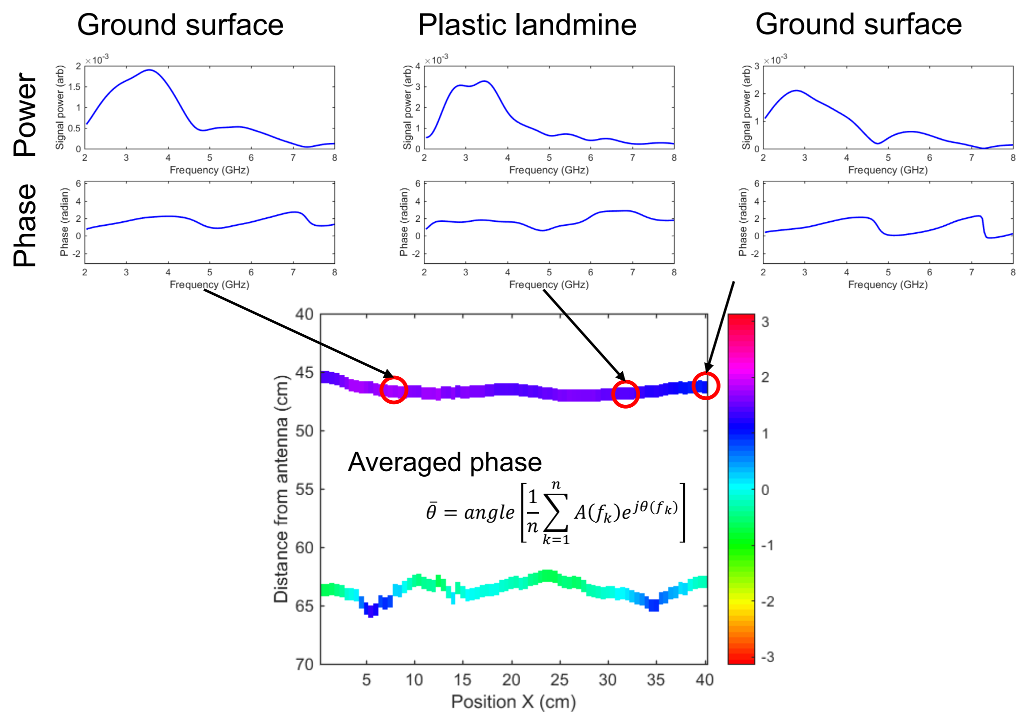

Fig. 5: Averaged phase values put at the first and second peak depths (bottom) and the original peak phase-profiles at some spatial points (top).

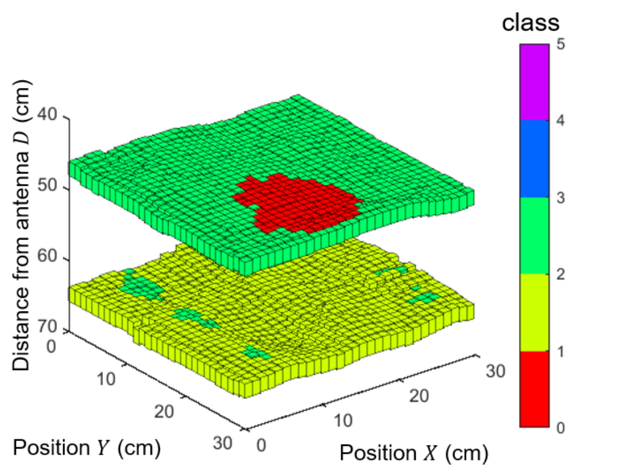

Fig. 6: Result of three dimensional grouping when considering the first and second peaks in our proposed PP-CSOM method [15].

clear peaks in D direction, corresponding to almost the surface of the soil and the bottom of the soil box. We find these peaks are broad. The phase changes mostly along the depth D, but with irregular changes at many local areas. It is interesting that we find several phase singular points, where the phase value shows non-zero rotation value but mostly $\pm 2\pi$ value). This is a feature specific to GPRs different from air/space radars.

The bottom color figure in Fig. 5 shows the averaged phase calculated by (1) for the two depth peaks at each position.

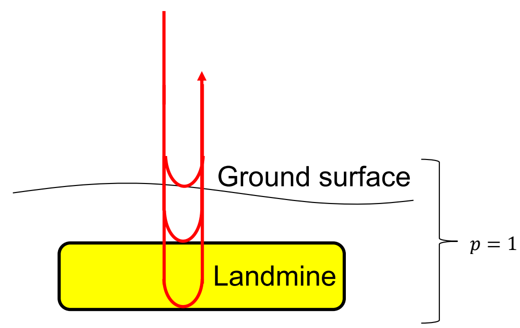

Fig. 7: Conceptual illustration explaining the scattering mechanism including multiple scattering resulting in frequency-dependent phase values.

The surface curve presents mostly violet color, resulting in difficulty in landmine detection. That is, the conventional PR method does not work effectively. However, the top three profiles clearly depends on the landmine or absence thereof. Our proposed PP-CSOM focuses on this difference.

We use the CSOM for the adaptive grouping of the peak phase-profiles (PP). We move the antennas two-dimensionally to obtain two peaks, $p = 1$ and 2, at each position (x, y). We clip respective peaks and move them to the time origin $t = 0$, apply Fourier transform, and obtain the frequency profile $\boldsymbol{k}_p$ to be fed to the CSOM. Here we prepare five classes for the grouping.

Fig. 6 presents the result of the PP-CSOM grouping for the two peaks at each location (x, y) sweeping over the observation area. We find a clear red area indicating a landmine.

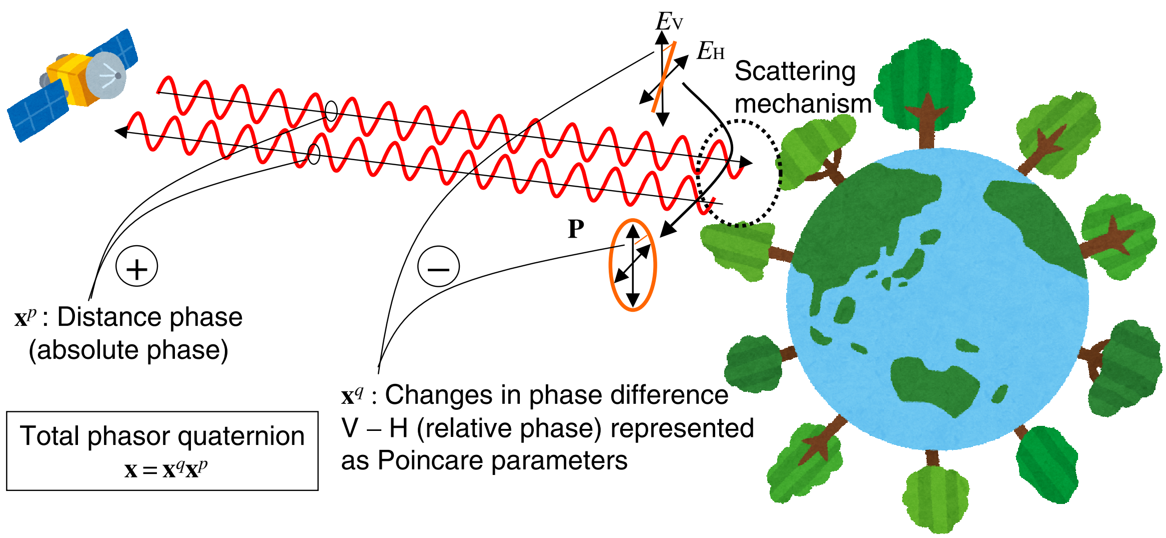

Fig. 8: Absolute and relative phase components represented by the phasor and quaternion parts, respectvely, of phasor quaternion in PolInSAR observation [23].

We can identify the landmine position with a consistent shape. The result clearly demonstrates the high performance of the PP-CSOM visualization method.

IV. Phase changes caused by sacttering

When we consider that the scattering occurs at sudden changes in the permittivity and/or conductivity underground, the phase change value should be 0 or π independent of the observation frequency. However, when the electromagnetic wave penetrates into a landmine and results in multiple scattering, the frequency profile can be complex. Fig. 7 illustrates the origin of the frequency-dependent scattering profile. In addition, the present case also include the soil surface in the multiple scattering. That is why we find a significance in the use of the high-dimensional profile in the PP as it is, instead of the average in the conventional PR. Therefore, it is also very important to separate the scattering phase profile from the propagation phase changes.

This idea is commonly shared with our another proposal, namely, phasor-quaternion neural networks (PQNN) effectively working in the singular-point removal in polarimetric-interferometric synthetic aperture radar (PolInSAR) in the field of satellite-borne/airborne SAR observations as illustrated in Fig. 8 [23]. It is also shared in the polarimetric GPR, where we use PQSOM [25]. There we deal with the scattering polarization changes and the propagation phase explicitly by the use of PQSOM [24]. In this sense, the polarization is the relative phase.

In contrast, the propagation phase represents the distance between the transmitter/receiver and the target. It can be called the absolute phase. The PQNN deals with these two entities (relative and absolute phase values) explicitly in a separate manner. The essential idea is shared in PP-CSOM. Accordingly, the separation of the relative scattering phase from the absolute propagation phase holds a significance in distinction and visualization of scatterers.

V. Conclusion

This paper investigated the essence of PP-CSOM processing to find that the separation of scattering phase from the propagation phase is essential in the visualization of scatterers. Most of conventional radars did not pay attention to phase profile in the time domain. However, the amplitude peaks show the scatterers' depths while the phase profiles represent scattering mechanisms. The latter is highly informative in the distinction and visualization of the scatters. We also discussed the fact that this idea is commonly shared by the phasor-quaternion neural-network (PQNN) processing, which is effective in polarimetric radar imaging. The explicit separation of the relative scattering phase and the absolute propagation phase will become more and more essential in polarimetric-interferometric radar imaging systems in the near future.

Acknowledgment

This work was supported in part by JSPS KAKENHI Grant Number 18H04105, and in part by the Tohoku University RIEC Cooperative Research Project.

References

[1] D. J. Daniels, *Ground penetrating radar*. IET, 2004, IEE radar, sonar, navigation, and avionics series, vol. 1.

[2] M. Sato, J. Fujiwara, X. Fenga, and T. Kobayashi, "Dual sensor alis evaluation test in Afghanistan," *IEEE Geoscience and Remote Sensing Society Newsletter*, pp. 22–24, Septermber 2005.

[3] T. Hara and A. Hirose, "Adaptive plastic-landmine visualizing radar system: effects of aperture synthesis and feature-vector dimension reduction," *IEICE Transactions on Electronics*, vol. E88-C, no. 12, pp. 2282–2288, 2005.

[4] E. Koyama and A. Hirose, "Development of complex-valued self-organizing-map landmine visualization system equipped with moving one-dimensional array antenna," *IEICE Transactions on Electronics*, vol. E101C, no. 1, pp. 35–38, January 2018.

[5] D. Seyfried and J. Schoebel, "Stepped-frequency radar signal processing," *Journal of Applied Geophysics*, vol. 112, pp. 42–51, 2015.

[6] M. Grasmueck and R. Weger, "3D GPR reveals complex internal structure of Pleistocene oolitic sandbar," *The Leading Edge*, vol. 21, no. 7, pp. 634–639, 2002.

[7] W. Zhao, E. Forte, F. Fontana, M. Pipan, and G. Tian, "GPR imaging and characterization of ancient Roman ruins in the Aquileia Archaeological Park, NE Italy," *Measurement*, vol. 113, pp. 161–171, 2018.

[8] S. Kadioglu, "Photographing layer thicknesses and discontinuities in a marble quarry with 3D GPR visualisation," *Journal of Applied Geophysics*, vol. 64, no. 3-4, pp. 109–114, 2008.

[9] W. W. Lai, R. K. Chang, J. F. Sham, and K. Pang, "Perturbation mapping of water leak in buried water pipes via laboratory validation experiments with high-frequency ground penetrating radar (GPR)," *Tunnelling and Underground Space Technology*, vol. 52, pp. 157–167, 2016.

[10] T. Hara and A. Hirose, "Plastic mine detecting radar system using complex-valued self-organizing map that deals with multiple-frequency interferometric images," *Neural Networks*, vol. 17, no. 8-9, pp. 1201–1210, 2004.

[11] Y. Nakano and A. Hirose, "Taper-walled linearly tapered slot antenna," *IEEE Journal of Selected Topics in Applied Earth Observations and Remote Sensing*, vol. 4, no. 4, pp. 779–784, April 2011.

[12] S. Onojima, Y. Arima, and A. Hirose, "Millimeter-wave security imaging using complex-valued self-organizing map for visualization of moving targets," *Neurocomputing*, vol. 134, pp. 247–253, 2014.

[13] V. G. Sugak and A. V. Sugak, "Phase spectrum of signals in ground-penetrating radar applications," *IEEE Transactions on Geoscience and Remote Sensing*, vol. 48, no. 4, pp. 1760–1767, 2010.

[14] V. Sugak and A. Sugak, "SFCW GPR sensor with phase processing for landmine detection and recognition," in *Physics and Engineering of Microwaves, Millimeter and Submillimeter Waves (MSMW), 2013 International Kharkov Symposium on*. IEEE, 2013, pp. 294–296.

[15] S. Shimomura and A. Hirose, "Adaptive subsurface 3-D imaging based on peak phase-retrieval and complex-valued self-organizing map," *IEEE Geoscience and Remote Sensing Letters*, vol. 17, no. 1, pp. 52–56, January 2020.

[16] A. Hirose, *Complex-Valued Neural Networks, 2nd Edition*. Heidelberg, Berlin, New York: Springer, 2012.

[17] S. Shimomura and A. Hirose, "Adaptive subsurface visualization system using phase retrieval method and complex-valued self-organizing map," in *Progress In Electromagnetics Research Symposium (PIERS) 2018 Toyama*, August 2018, p. 476.

[18] ——, "Target clustering in three-dimensional ground penetrating radar based on time-domain phase information and complex-valued self-organizing map," in *IEEE International Geoscience and Remote Sensing Symposium (IGARSS) 2019*, 2019, pp. 3602–3625.

[19] Y. Otsuka, T. Shimada, R. Natsuaki, and A. Hirose, "Consideration on singular-point generating mechanisms by analyzing the effect of phase-and-polarization optimization in polinsar," *IEEE Journal of Selected Topics in Applied Earth Observations and Remote Sensing*, vol. 13, no. 4, pp. 1625 – 1638, 2020.

[20] H. Kim and A. Hirose, "Unsupervised fine land classification using quaternion auto-encoder-based polarization feature extraction and self-organizing mapping," *IEEE Transactions on Geoscience and Remote Sensing*, vol. 56, no. 3, pp. 1839–1851, March 2018.

[21] Y. Otsuka, R. Natsuaki, and A. Hirose, "Enhancement of polarization mechanism in pixel-by-pixel phase optimization in PolInSAR," in *IEEE International Geoscience and Remote Sensing Symposium (IGARSS) 2019 Yokohama*, July 2019, pp. 5706–5709.

[22] Y. Otsuka, T. Shimada, R. Natsuaki, and A. Hirose, "Analysis of singular-point generating mechanisms based on the correlations among the parameters in coherency matrix and those in the optimized scattering-mechanism vector in polinsar," in *Progress in Electromagnetics Research Symposium (PIERS) 2018 Toyama*, 2018, p. 474.

[23] A. Hirose, "Phasor quaternion neural network framework and its significance in Big SAR intelligence," in *International Conference on Emerging Techniques in Computational Intelligence (ICETCI) 2021*, ser. to be presented, 2021.

[24] Y. Song and A. Hirose, "Phasor-quaternion self-organizing-map-based ground penetrating radar systems," *IEEE Transactions on Geoscience and Remote Sensing*, to appear 2021.

[25] ——, "Proposal of a ground penetrating radar system utilizing polarization information by using phasor-quaternion self-organizing map," in *International Geoscience and Remote Sensing Symposium (IGARSS) 2021*, ser. to be presented, 2021.

[26] T. Kohonen, "The self-organizing map," *Proceedings of the IEEE*, vol. 78, no. 9, pp. 1464–1480, 1990.

[27] S. Masuyama and A. Hirose, "Walled LTSA array for rapid, high spatial resolution, and phase-sensitive imaging to visualize plastic landmines," *IEEE Transactions on Geoscience and Remote Sensing*, vol. 45, no. 8, pp. 2536–2543, 2007.

[28] S. Masuyama, K. Yasuda, and A. Hirose, "Multiple-mode selection of walled-LTSA array elements for high-resolution imaging to visualize antipersonnel plastic landmines," *IEEE Geoscience and Remote Sensing Letters*, vol. 5, no. 4, pp. 745–749, 2008.

[29] Y. Nakano and A. Hirose, "Improvement of plastic landmine visualization performance by use of ring-CSOM and frequency-domain local correlation," *IEICE Transactions on Electronics*, vol. 92, no. 1, pp. 102–108, 2009.

[30] T. Aoyagi, D. Radenamad, Y. Nakano, and A. Hirose, "Complex-valued self-organizing map clustering using complex inner product in active millimeter-wave imaging," in *International Joint Conference on Neural Networks (IJCNN) 2010*. IEEE / INNS, 2010, pp. 1–6.

[31] A. Hirose and S. Yoshida, "Generalization characteristics of complex-valued feedforward neural networks in relation to signal coherence," *IEEE Transactions on Neural Networks and Learning Systems*, vol. 23, pp. 541–551, 2012.

[32] N. Jastram and D. S. Filipović, "Wideband millimeter-wave surface micromachined tapered slot antenna," *IEEE Antennas and Wireless Propagation Letters*, vol. 13, pp. 285–288, 2014.